



Novel zwitterion functionalized carbon nanotube nanocomposite membranes for improved RO performance and surface anti-biofouling resistance



Wai-Fong Chan, Eva Marand, Stephen M. Martin*

Department of Chemical Engineering, Virginia Polytechnic Institute and State University, 245 Goodwin Hall, Blacksburg, VA 24061, USA

ARTICLE INFO

Article history:

Received 4 August 2015
Received in revised form
15 January 2016
Accepted 7 February 2016
Available online 24 February 2016

Keywords:

Carbon nanotube
Thin film nanocomposite
Zwitterion
Reverse osmosis
Biofouling

ABSTRACT

Zwitterion functionalized carbon nanotubes (CNTs) were incorporated into polyamide thin film composite membranes to improve membrane permselectivity and surface biofouling resistance. The CNTs within the polyamide layer were partially aligned via a vacuum filtration step during membrane synthesis, and the fabrication of the zwitterionic CNT/polyamide nanocomposite membranes was optimized by varying the loadings of CNTs and the crosslink density of the polyamide. The permeation flux was found to increase by approximately three-fold as the fraction of CNTs was increased from 0 to 20 wt% for all the salt solutions tested in our study. The steric hindrance to transport due to the zwitterionic functional groups prevents the permeation of the majority of ions through the CNT pores, resulting in high salt rejection. The charges of the zwitterionic groups do not appear to produce a significant Donnan potential to reject ions, and thus surface charge had no effect on membrane selectivity. The semi-aligned zwitterionic CNTs appeared to be exposed at the membrane surface and interacted with the feed water to form a strong hydration layer, resulting in improved surface biofouling resistance. The adsorption rate of protein foulants on the nanocomposite membrane surface was significantly reduced compared to the control membrane without CNTs, and the adsorbed fouling layer could be easily removed by flushing with water. After washing, the nanocomposite membrane recovered 100% of the decreased water flux whereas the control membrane only recovered 10% of the decreased flux resulting in a permanent loss of 30% in water permeation.

© 2016 Elsevier B.V. All rights reserved.

1. Introduction

The demand for fresh water is rising globally and the trend has accelerated continuously in the past decade accompanied with population overgrowth, rapid industrialization in developing countries, contamination of available water resources, and climate change [1]. However, the supply for fresh water is not sustainable with current global development, and more than one-third of the world's population is currently living in water-stressed countries [2]. Reverse osmosis (RO) is the leading desalination technique and can alleviate global water scarcity by retrieving high quality of fresh water from non-drinkable water resources (i.e. sea, brackish and waste water) [3]. Desalination by RO is expected to reach 38 billion m³ per year by 2016 [2], which is nearly 1% of global fresh water consumption. Aromatic polyamide (PA) based thin film composite membranes (TFC) are the main type RO membranes currently in use [4–6]. Many recent studies have focused on

modifying TFC membranes to achieve high energy-efficiency, ultra-low surface fouling and robustness against chemical attack. While industries have developed different types of membrane materials to target these problems separately, nanotechnology provides a new route to address the issues at the same time. By building novel membranes with either internal nano-structures (i.e. nanopores) or incorporation of nanoparticles or nanotubes, size sieving can be achieved down to sub-nanometer scales, and can render membranes resistant to reactive chemicals and surface protein adsorption [7–10].

Among the choices of nanomaterials, carbon nanotubes (CNT) show promising results as building blocks for nano-engineered membranes. Computational and experimental studies of fluid transport through CNT pores have demonstrated significantly higher fluxes than in other nanoporous materials due to their smoothness and regularity [11–13]. Molecular dynamics (MD) simulation studies [14,15] have examined water and ion transport through CNTs with a range of pore sizes through which water passes rapidly but ions do not. These studies demonstrate that the degree of selectivity towards different ion types varies with pore radius, and pores of radius ranging from 3.4 to 6.1 Å exhibit

* Corresponding author.

E-mail addresses: wchan6@vt.edu (W.-F. Chan), martinsm@vt.edu (S.M. Martin).

rejection of even monovalent ions. CNTs with functional groups attached at both ends were also explored computationally and exhibited outstanding filtration ability [16]. Tip functional groups reduce the CNTs' effective pore size, granting separation ability to CNTs with larger diameters, potentially decreasing materials costs. Functional groups improve dispersion and the compatibility of CNTs in composite materials and minimizes defects during membrane synthesis [17–19]. Membranes with vertically-aligned CNTs (VACNT) embedded in a polymer composite were synthesized experimentally, with inner diameters ranging from 1.6 to 10 nm [10,11,20,21]. As expected, liquid flow through the non-interacting hydrophobic cores of the CNT is found to be significantly enhanced, with velocities at least 1000 times faster than that predicted by conventional no-slip hydrodynamic theory [13,22]. The ion rejection in these membranes, however, is often provided by the functional groups attached at the CNTs' opening rather than sieving by the size of the CNT pores. Fornasiero et al. studied ion exclusion in CNTs functionalized with hydroxyl, carbonyl and carboxylic groups [10], and their results demonstrated that rejection was dominated by electrostatic interactions between the fixed COO^- charges on the ends of CNTs and the co-ions in the feed. This is a Donnan-type exclusion mechanism and is subject to electrostatic screening effects at higher electrolyte concentrations, leading to a total loss of rejection ability. In addition, the fabrication of CNT-based nanocomposite membranes often involves sophisticated in-situ processes like surface etching [11] which is not easily scalable for large scale manufacturing.

Thin-film-nanocomposite (TFN) membranes employ a different approach to building novel RO membranes. Nanomaterials such as zeolite, silver and titanium oxide particles, silica and CNTs with excellent properties (e.g., super-hydrophilicity, fast water transport, and biocide) are directly blended in the PA skin layer and dispersed within the polymer matrix to enhance membrane permselectivity or introduce new properties [9,17,18,23–27]. Many researchers reported improved performance (Table 1) in terms of water permeation flux and fouling resistance, but the degree of crosslinking of the polymer skin layer is reduced during the process, leading to a decrease in selectivity and mechanical stability. For better comparison of the water flux in different membrane systems, the pure water permeability (PWP) was calculated using Eq. (1) for each membrane shown in Table 1. J_p is the permeation flux in the units of liters per square meter per hour (LMH), and ΔP and $\Delta \Pi$ are the applied transmembrane and osmotic pressures, respectively.

$$\text{PWP} = J_p / (\Delta P - \Delta \Pi) \quad (1)$$

As shown in Figs. 1 and 2, all-aromatic polyamides are chemically crosslinked to form rigid chains with self-assembled networks of pores for water uptake and transport [28]. When nanomaterials, illustrated as spheres A and B in Fig. 2, are present during the polymerization, part of the crosslink network is disrupted when polymer end groups were prevented from reacting with other monomers and were terminated with carboxylic acid groups. When crosslinking is possible by detouring around the nanomaterials, the rigid aromatic backbones in PA restrict the segmental motion of chains. The lack of chain rotation results in nanosized defects (shown as blue ovals in Fig. 2) around the sphere surface and also lowers the selectivity. Nanomaterials that are incompatible with polyamide (sphere B in Fig. 2) open up larger defects and destroy the stability of the layer. A performance comparison can be seen in Table 1. Ordinary PA membranes exhibit salt rejections as high as 99.8%, but all the reported TFN membranes fall below this value. All the PA fabrication methods shown in the table use the same monomeric aromatic amines and crosslinking agent, with different recipes in terms of pH in monomer solution, cure temperature, crosslinking time, etc. Kim et al. demonstrated the impact of the interaction between nanomaterials and the PA on the membrane selectivity [18]. Functionalized CNTs with higher interaction forces with Atomic Force Microscopy (AFM) tips coated with PA film exhibited improved water flux and salt rejection when added into the PA layer, when compared to other types of CNT with lower interaction forces.

A thin, durable and scalable nanocomposite membrane with properties that can operate at high salt concentration is highly desirable. Previous work in our laboratory has focused on using zwitterion-functionalized single-walled CNTs (Z-SWNT) as the nanomaterial in fabricating TFN membranes [17]. The alternation of charges in the zwitterion results in a very strong dipole moment, which greatly enhances the interaction between the Z-SWNT and the PA matrix. Moreover, zwitterion-treated surfaces have also shown good resistance to protein adhesion in several studies [35–37]. MD simulations have predicted that CNTs having a diameter of 1.5 nm with two or more zwitterionic groups attached at both ends reject salt ions completely [17]. We have previously reported the synthesis of PA membranes embedded with a high weight percentage of partially-aligned Z-SWNT [17]. These membranes exhibited significant improvements in water permeation and similar or improved salt rejection as the weight percentage of the nanotubes in the membrane increased. Both simulation and experiment suggested that the zwitterionic groups act as a

Table 1
Research studies on thin film nanocomposite membranes using different nanomaterials.

Nanomaterials	Applied pressure (MPa)	Permeation flux (L/(m ² h))	Pure water permeability (L/(m ² h bar))	Rejection (%)	Advantages
No additive [29]	1.55	43.0	2.9	99.8	
Multi-walled CNT; ~8 nm inner diameter [30]	0.69	22.0	3.4	92.1	<ul style="list-style-type: none"> Applied potential significantly increases fouling resistance 1 min-flushing can recover almost 92% of flux.
Zeolite A nanoparticles [31]	1.24	16.5	1.4	91.2	<ul style="list-style-type: none"> Increases surface hydrophilicity Improves water permeability, solute rejection and fouling resistance.
Linde type A (LTA) zeolite nanocrystals [32]	1.55	108.8	7.4	90	<ul style="list-style-type: none"> Reduces polymer cross-linking Microporous defects were observed
Titanium oxide (TiO ₂) [33]	0.60	9.1	1.6	95 ^a	<ul style="list-style-type: none"> Enhances hydrophilicity; higher water flux
Silver nanoparticles [9]	1.38	90	6.7	96.5 ^a	<ul style="list-style-type: none"> Colonies of Pseudomonas on membrane surface were almost all dead.
Polyhedral Oligomeric Silsesquioxane (POSS) [34]	1.55	27.5	1.9	~98	<ul style="list-style-type: none"> Acts as cross-linkers and increases free volume of the PA film, which thus increases permeation.

^a Salt in the feed solution is magnesium chloride (MgCl₂).

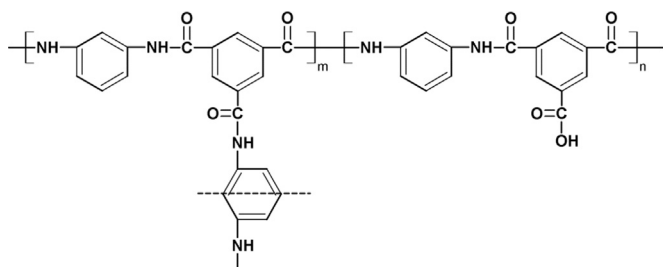


Fig. 1. Polymer structure of all-aromatic polyamide in thin-film composite RO membrane.

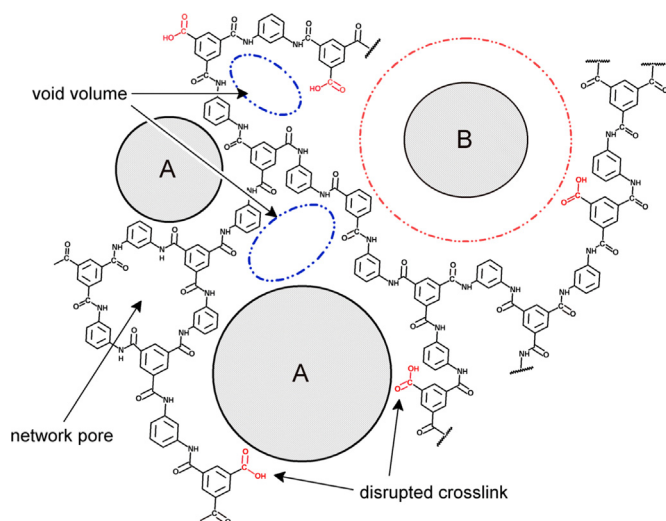


Fig. 2. Schematic illustrates the disruption of PA chains in TFN membranes when nanomaterials (sphere A and B) present in the skin layer. Sphere A is chemically compatible to PA but B is not due to poor interfacial interaction. The red circle represents the closest distance PA chains can be around sphere B. (For interpretation of the references to color in this figure legend, the reader is referred to the web version of this article.)

gatekeeper at the entrance of the CNTs, rejecting ions via steric effects instead of charge repulsion. Herein we report on the impact of chemical structure, surface morphology, and separation mechanism on the performance of Z-SWNT/PA TFN membranes. We also report on improved resistance to surface biofouling in the TFN membranes due to the incorporation of Z-SWNTs.

2. Materials and methods

2.1. Materials

The following chemicals were purchased from Sigma-Aldrich (St. Louis, MO): 1,3,5-benzenetricarbonyl trichloride (trimesoyl chloride, TMC), 1,3-phenylenediamine (m-phenylenediamine, MPD) and sodium dodecylbenzenesulfonate (SDBS). D-(+)-raffinose pentahydrate, α -cyclodextrin, D-(+)-galactose, D-(+)-maltose monohydrate and β -D-lactose were purchased from Alfa Aesar (Ward Hill, MA). Methanol was purchased from Fisher Scientific (Hampton, NH), cyclohexanone from Cole-Parmer (Vernon Hills, IL), and bovine serum albumin (BSA) from BioWorld Inc. (Dublin, OH). Alginic acid, sodium salt (AAS) was from Scientific Polymer Products, Inc. (Ontario, NY). All chemicals were used as received without further purification. Polyethersulfone (PES) ultrafiltration membranes were provided by Trisep Corporation (Goleta, CA). The salts used in this study were potassium chloride (KCl; FisherChemical), sodium chloride (NaCl; Sigma-Aldrich), magnesium chloride hexahydrate ($\text{MgCl}_2 \cdot 6\text{H}_2\text{O}$; EK industries), magnesium

sulfate (MgSO_4 ; Spectrum Chemical MFG. Corp.) and calcium chloride (CaCl_2 ; Sigma-Aldrich).

2.2. CNT functionalization

Carboxylate functionalized SWNTs of outer diameter 15 Å and length 1 μm were purchased from Nano Lab Inc. (Waltham, MA) [38]. We used the same functionalization procedure described in our prior work [17,39]. The COOH functionalized SWNTs were produced by chemical vapor deposition (CVD). The concentration of -COOH groups in the SWNTs was reported by the manufacturer to be between 2 and 7 wt-% (as determined by titration). However, the concentration of -COOH groups was determined to be 21.6 wt% as calculated from the atomic percentage of oxygen determined via x-ray photoelectron spectroscopy (see [Supplementary material](#)). This value assumes that all oxygen atoms were located in -COOH groups. The functionalized SWNTs were reacted with thionyl chloride (SOCl_2) at 65 °C for 36 h and the -COOH groups were replaced by COCl groups. The acylated SWNTs were then esterified using 3-dimethylamino-1-propanol, $(\text{CH}_3)_2\text{N}-\text{C}_3\text{H}_6-\text{OH}$. This was followed by a ring-opening reaction of lactone, in which β -propiolactone was opened to form an acid group and attached to the tertiary amine on the functional group [39,40]. The resulting zwitterionic group had a positive charge at the tertiary amine group and a negative charge at the carboxylated group. The final chemical structure is illustrated in [Fig. 3](#). The zwitterion content was determined to be 25.2 wt% by XPS (see [Supplementary material](#)). This corresponds to ~ 2 zwitterion groups for every 100 carbon atoms in the CNT.

2.3. Membrane fabrication

The interfacial polymerization (IP) of polyamide is very sensitive to operating conditions and reaction time. Different publications report different recipes in terms of the concentration of monomers, contact time, air-drying time, curing temperature, etc. [29,41–43]. Our fabrication process was divided into two steps: deposition and alignment of CNTs, and interfacial polymerization of PA, as shown schematically in [Fig. 4](#). The PES support used in this fabrication was first immersed in a 0.5 wt% SDDBS solution for two days and then in deionized (DI) water for one more day to open the pores and increase the hydrophilicity. A predetermined quantity of zwitterion functionalized SWNTs were dispersed in DI water through ultrasonication. The pretreated PES membrane was placed in the filtration system and the dispersed Z-SWNTs solution was poured on top of it. We then used vacuum filtration to deposit the SWNTs on the support, to provide some alignment, [44] and to remove the solvent. The SWNT coated support was then dried for an hour in a vacuum oven to insure that all water was removed from the nanotubes and the support pores before interfacial polymerization (IP) took place.

The second step in the membrane fabrication process was interfacial polymerization of PA. The SWNT coated PES support was

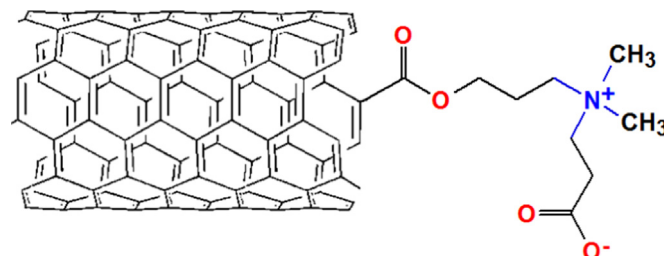


Fig. 3. Schematic of the chemical structure of zwitterionic functional group attached on the SWNTs.

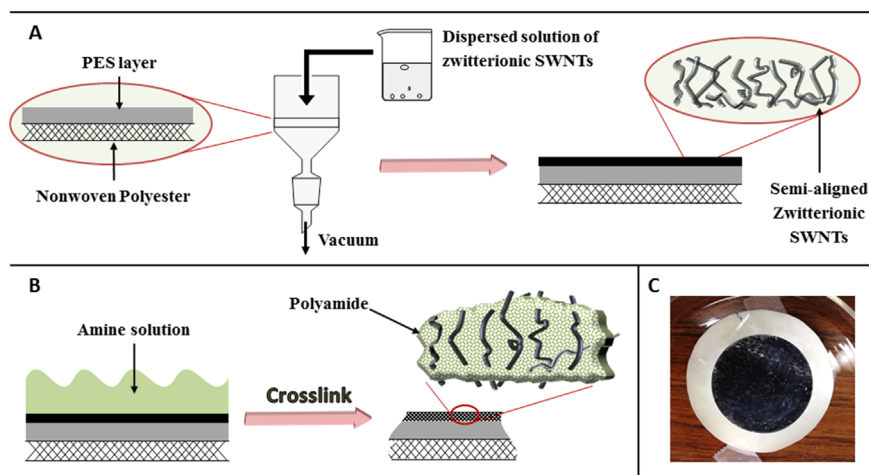


Fig. 4. Cross-sectional schematics of the fabrication procedure for Z-SWNT/PA nanocomposite membrane. (A) PES ultrafiltration membrane is composed of a thin PES layer covered on a non-woven polyester web, and has been pretreated in surfactant solution. Zwitterion functionalized SWNTs were then deposited onto the PES membrane support through vacuum filtration. (B) Aromatic polyamide formed in between the semi-aligned functionalized SWNTs via interfacial polymerization, at which aqueous solution containing MPD monomers came in contact with nonaqueous solution containing TMC crosslinker. (C) Photograph of the top of Z-SWNT nanocomposite membrane that is the effective side exposed to the feed solution.

sandwiched between two circular poly(tetrafluoroethylene) (PTFE) frames. IP was carried out on the support by wetting the SWNT coated side with an aqueous diamine solution containing 2 wt% MPD and 0.2 wt% of SDBS at ambient temperature for 2 min. The membrane was then unclamped from the PTFE frames and immediately placed on a glass plate. A glass roller was used to roll over the membrane to remove all the excess MPD solution. The membrane was then sandwiched again between the frames and wetted by an n-hexane solution containing 0.34% (v/v) TMC for 90 s. The resulting PA thin film nanocomposite membrane was then heat cured at 68 °C for 5 min. After the membrane had cooled down, it was washed thoroughly with DI water, submerged in fresh DI water and stored in a laboratory refrigerator at 4 °C.

2.4. Membrane characterization

The surface roughness of the membranes was measured by Atomic Force Microscopy (AFM; Asylum Research[®] Cypher scanning probe microscope) using contact mode, with a 5 μm^2 scanned area. The roughness parameters were estimated from the AFM images and calculated with the AFM surface analysis software (MFP-3D, Igor Pro v.6.3.4.1). The surfaces and cross-section of the membranes were characterized using field emission scanning electron microscopy (FESEM, LEO 1550). Membrane samples were prepared for SEM cross-section imaging by gently peeling away the polyester backing fabric while ensuring the PES and Z-CNTs/PA layers remained together. A small piece of fabric-free membrane sample was then frozen in liquid nitrogen and fractured cryogenically. The hydrophilicity of the membrane surface was measured through contact angle experiments (KSV Instruments LTD Cam 200) using test droplets composed of deionized water. Static water contact angles were determined from side-view pictures captured after the value of contact angle stabilized. The chemical structure of the plain polyamide and Z-SWNT nanocomposite membranes were characterized by attenuated total reflectance Fourier transform infrared spectroscopy (ATR-FTIR; Varian 670-IR FT-IR Spectrometer). Spectra were collected in air in the mid-infrared region (800–4000 cm^{-1}), using 256 scans at resolution 1 (0.4821 cm^{-1} spacing). Before each measurement, a background spectrum was obtained and subtracted from that of the membrane to remove any atmospheric absorbance peaks.

2.5. Membrane permeation test

Pressure-driven permeation experiments were carried out on a laboratory-scale cross-flow membrane test unit, shown schematically in Fig. 5, capable of withstanding pressures from 0.17 to 6.9 MPa. This test unit is comprised of a 316 stainless steel membrane cell, a high pressure pump (Hydra-cell pump, Warner Engineering), and a feed tank operated in closed loop mode with the retentate being circulated back to the feed water reservoir. Feed solutions contained common cations (Na^+ , Mg^{2+} , K^+ and Ca^{2+}) at predetermined concentrations, and were kept at room temperature by a temperature controlled chiller (VMR; 1150S). The applied transmembrane pressure and the circulation flow rate were adjusted to 2.41 MPa and 2.5 L/min, respectively. The permeation flux was allowed to equilibrate for 30 min before any permeant collection. A known amount of permeant was collected in a glass vial within a given period of time. The density of water was taken to be 0.997 g/cm^3 at ambient temperature, the volumetric flow rate was calculated from $Q = \frac{\Delta V}{tA}$, where ΔV is the permeate volume (liter), t is the permeation time (hours) and A is the effective membrane area (m^2). The flow rate, Q , was then calculated in the units of liter per square meter per hour (LMH). The concentration analysis of the cations present in the permeant was measured by atomic adsorption spectrophotometry (AAS; Perkin Elmer 5100, Wellesley, MA). The concentrations of cations in the feed, C_f , and the permeant, C_p , were then measured and used to calculate salt rejections using the equation shown below.

$$\mathfrak{R}(\%) = \left(1 - \frac{C_p}{C_f} \right) * 100 \quad (1)$$

2.6. Pore size distribution test

The pore size distribution in the RO membranes was measured using the method developed by Otero et al. [45] as follows: eight solutes (i.e., methanol, ethanol, cyclohexanone, galactose, lactose, maltose, raffinose, and α -cyclodextrin) with different Stokes' radii were each dissolved in DI water to prepare different feed solutions with concentrations of 500 ppm. The testing conditions and procedure were identical to the cross-flow filtration test described in the previous section. The concentration of carbon content in the feed and permeate solution were measured by a total organic

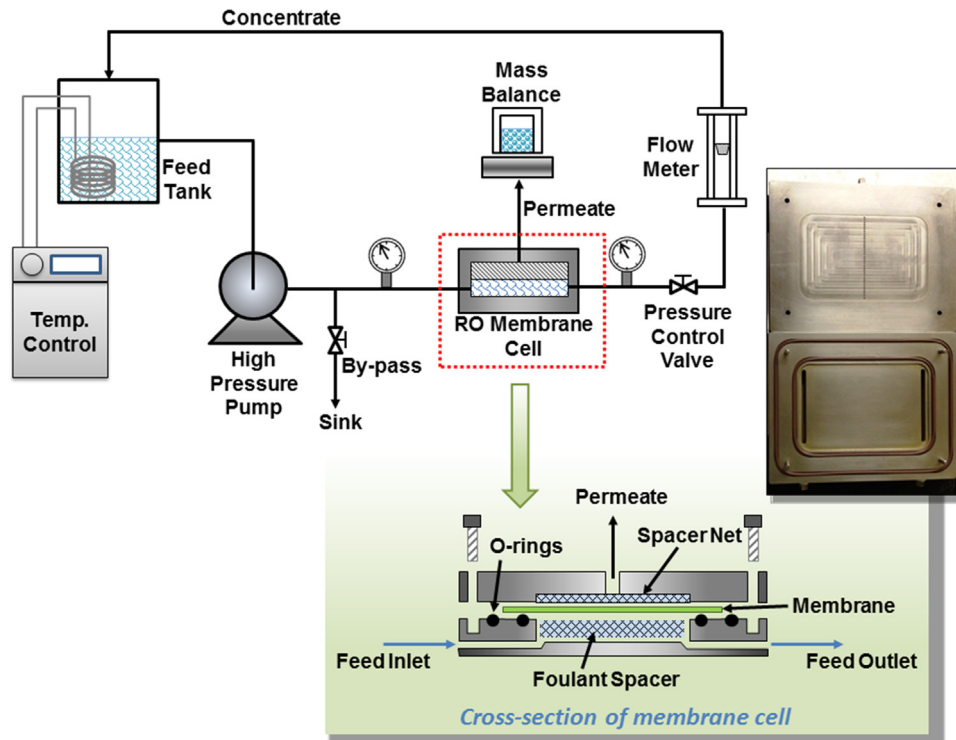


Fig. 5. Schematic diagram of the RO membrane system and the cross-section of membrane test cell. The photograph on the right is the stainless steel cell, where the upper half is the permeation side and the lower part is the feed side.

carbon (TOC) analyzer to obtain the rejection. The results were analyzed using the equation

$$f = J_{W,t} / J_W = 1 - \frac{1}{1 + \left(\frac{r_p}{B}\right)^C} \quad (2)$$

where f and r_p are the number fraction of pore size and pore size, respectively. $J_{W,t}$ and J_W are the pure water flux passing through the transmitting pores and the total pure water flux, respectively. B and C are constants that were obtained through non-linear fitting of the permeation data using Origin 9.0 software. In this study, the plot of $\frac{df}{dr}$ versus r was used to determine the pore size distribution of the RO membrane based on Eq. (2). A more detailed discussion of the pore size model is presented in the [Supplementary material](#).

2.7. Surface fouling experiment

A series of cross-flow filtration experiments were also conducted to investigate the surface fouling of the RO membranes. Initially, membrane samples were used to filter DI water for 12 h. Then a solution containing model organic foulants was introduced into the feed tank. The membrane permeation flux was then recorded for the next 10 h. BSA (model protein) and AAS (model polysaccharide) were the organic foulants added in the feed solution in different concentrations. BSA fouling has been proven to be significantly enhanced with the presence of AAS [46]. The temperature of the feed solution was kept at 20 ± 0.5 °C and the circulation flow rate was kept at 1.0 L/min for all the testing. The circulation flow was significantly slower than that in the ion filtration experiment in order to facilitate the adsorption of the foulant on the membrane surface. To obtain a better comparison across different membranes, the applied transmembrane pressure was adjusted from membrane to membrane so that all the trials have a similar initial permeation flux. When the fouling tests were

completed, the membranes were then washed again with water to determine their flux recovery capability. DI water was circulated in the RO system for 12 h with flow rate at 2 L/min under a transmembrane pressure of 0.34 MPa. After cleaning, the tank was refilled with new DI water and the filtration test continued for another hour under the same conditions as in the fouling test. The permeation flux after the wash was also recorded.

3. Results and discussion

3.1. Membrane morphology

The overall thickness of the skin layer of the Z-SWNT/PA membranes was reported in our prior publication [17] and was approximately 250 nm. AFM imaging of the membrane surfaces, depicted in Fig. 6, showed that the surface roughness increased significantly after polymerization of PA on the PES support. The root mean square deviation of the surface roughness increased from 5.86 nm to 27.03 nm after plain PA was coated on the support, and to 27.62 nm when both the functionalized SWNT and PA were coated on the support. The increased surface roughness was at least partly due to the ridge-and-valley microstructure of the PA coating, as shown previously [1,2,33,47], as well as in our SEM image in Fig. 6(B). The AFM image for Z-SWNT/PA has a very similar surface roughness to the control sample, thus it is difficult to tell whether the Z-SWNTs are exposed on the surface of the membrane. The surface contact angles of plain PA and nanocomposite membranes are shown in Table 2 and their values are also very close to each other. This suggests that the Z-SWNT/PA membrane surface is covered by PA, and that the addition of Z-SWNTs has little effect on the membrane surface. An ideal nanocomposite membrane, however, would have CNTs perfectly aligned with the direction of fluid flow and would percolate completely through the membrane, so that no fluid would have to permeate through the polymer matrix. The surface properties of

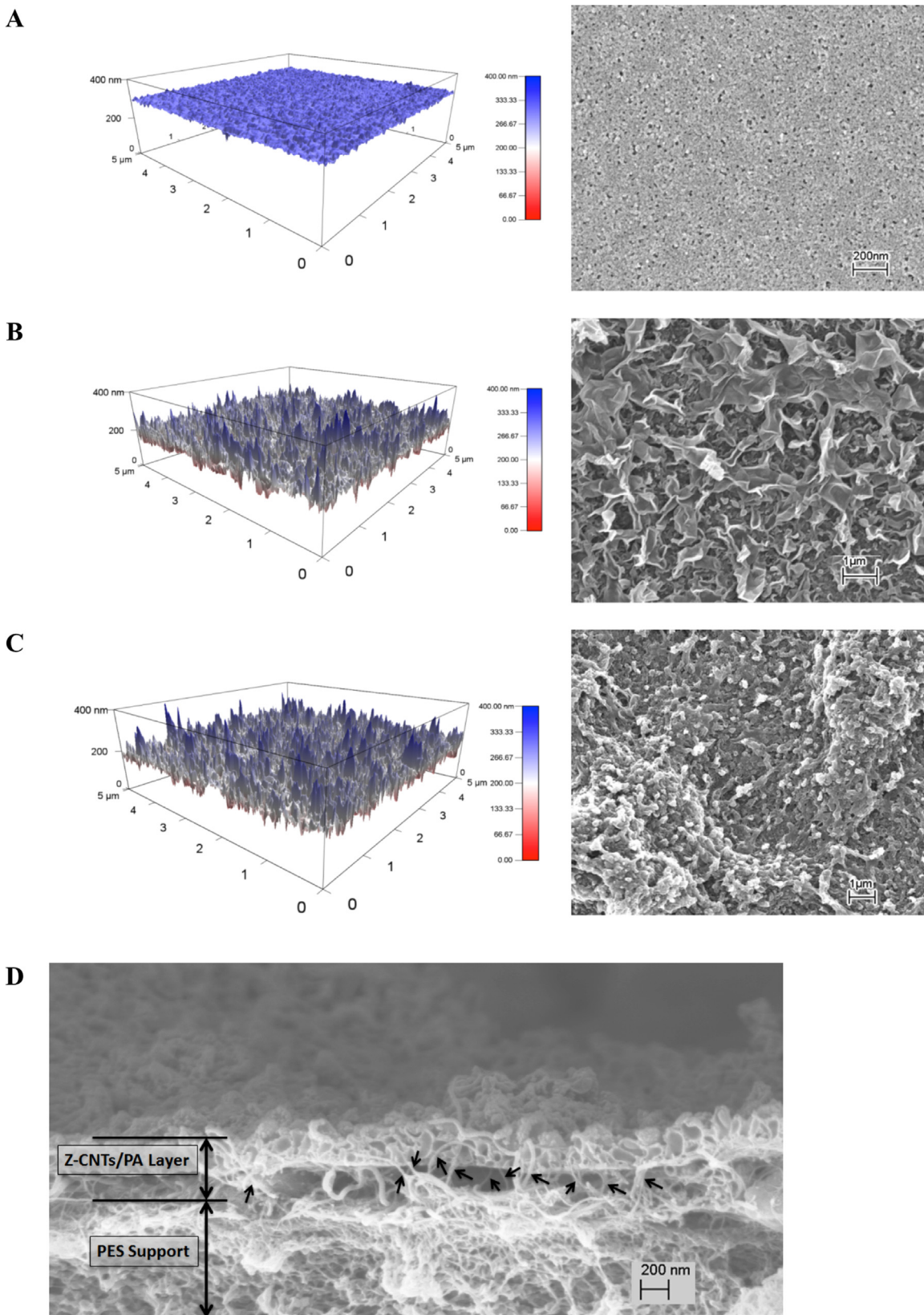


Fig. 6. AFM and SEM images of the surface of (A) polyethersulfone (PES) ultrafiltration membrane support, (B) plain polyamide membrane, and (C) 20 wt% Z-SWNT/PA membrane. The root mean square of surface roughness of (A), (B) and (C) are 5.86, 27.03 and 27.62 nm, respectively. (D) Shows the cross-sectional view of the Z-SWNT/PA membrane, where black arrows indicate the CNTs with semi-aligned orientation. SEM images are adapted with permission from ACS Nano [17].

such a membrane would be expected to be different from a PA coating. In contrast, SEM images (Fig. 6D) show that some bundles of SWNT percolate through the top of the PA layer and extend

above the surface. This could allow the tip functional groups on the CNTs to interact directly with the solutes dissolved in the feed solution, as demonstrated in protein fouling experiments (vide

Table 2
Contact angles for Z-SWNT, polyamide and 20 wt% Z-SWNT nanocomposite membrane.

Material	Contact angle ¹
Z-SWNT	90.9° ± 3.4°
Polyamide (PA)	61.6° ± 6.6°
20 wt% Z-SWNT/PA	66.5° ± 8.5°

^a (1) Reported errors are one standard deviation; (2) ANOVA analysis indicated no statistically significant difference between the contact angles of PA and Z-SWNT/PA ($F=0.62$).

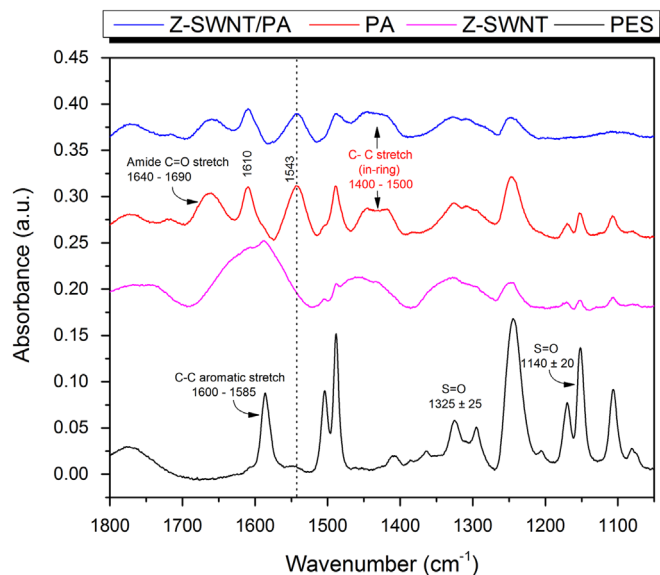


Fig. 7. Expanded view of ATR-FTIR spectra at the bonding stretch region (1800 to 1050 cm^{-1}). Spectra include PES support (black), Z-SWNT deposited on PES support (pink), plain PA membrane (red) and Z-SWNT/PA membrane (blue). The polymer structure of aromatic PA (top) and PES (bottom) are also shown in the graph for identification of their bonding. Dash line at 1543 cm^{-1} indicates the reference peak used for normalizing other bonding peaks for cross comparison. (For interpretation of the references to color in this figure legend, the reader is referred to the web version of this article.)

infra).

3.2. ATR-FTIR analysis

ATR-FTIR measurements were employed to analyze the chemical composition of the skin layer of the PA and Z-SWNT/PA membranes. The IR spectrum between wavenumbers 1800 and 1050 cm^{-1} is shown in Fig. 7, where it shows the bonding stretch of the signature peaks for the PES support with and without Z-SWNTs deposited on the surface, plain PA, and Z-SWNT/PA membranes. The spectrum of PES shows medium and strong S=O stretches at 1325 and 1140 cm^{-1} , which is a contribution from the sulfone group. After a thin layer of PA was coated on top of it, the S=O peaks diminished but strong amide C=O and aromatic amide C=C ring stretches were observed at 1660 and 1610 cm^{-1} . The N-H in-plane bending and N-C stretching vibration of the -CO-NH-group was also observed at 1543 cm^{-1} [30]. The spectrum of Z-SWNT/PA also contains the same strong amide peaks, showing that the nanocomposite membrane consists primarily of the PA matrix. A comparison of the in-ring C-C stretch (1500 to 1400 cm^{-1}) between PA and Z-SWNT/PA was conducted to quantify the addition of CNTs in the thin film. The signal for this

peak in the PA control sample is solely due to the aromatic structure of PA, whilst the signal in the TFN membrane contains contributions from both the ring structure in the SWNTs and the PA. The peak at 1543 cm^{-1} was chosen as a reference peak since it did not show up in the spectrum of the PES substrate (more discussion about the choice of the reference peak can be found in the Supplementary material). Following normalization with respect to the reference peak, the concentration of C-C (in-ring) stretch in Z-SWNT/PA membrane is 44.9% higher than that in the plain PA membrane. A broad peak due to the in-ring C-C stretch was also observed in Z-SWNT spectrum, suggesting that a high weight percentage of hexagonal carbon rings were introduced to the PA skin layer due to the addition of CNTs during the membrane fabrication process.

3.3. Composition study of the Z-SWNT/PA membranes

As discussed earlier, the degree of polyamide crosslinking can be disrupted easily by the presence of nanomaterials and this can reduce the high salt selectivity of the PA skin layer. By increasing the concentration of TMC, the concentration of the electrophilic carbonyl functional groups is increased in the solution, which initiates more local step-growth polymerization and forms low-molecular-weight homologs. The more homologs grown around the embedded nanomaterials, the higher the chance for these homologs to be crosslinked together to form a PA backbone close to the surface of the nanomaterials. Increased TMC increases the overall reaction rate and yields a higher degree of crosslinking at the end of the polymerization, and more importantly, it minimizes void volume formed at the interface between PA matrix and the nanomaterials. Increasing the TMC concentration also substantially increases the density of PA and forms a more durable but less permeable skin layer around the embedded nanomaterials [48]. A series of trade-off experiments were conducted to study the correlation between the loading of CNTs and the integrity of the nanocomposite skin layer by adjusting the concentration of Z-SWNTs deposited onto the membrane and the TMC content in the hexane solution. Fig. 8 depicts the permeation results for each membrane with the permeation flux tagged in the figure in the

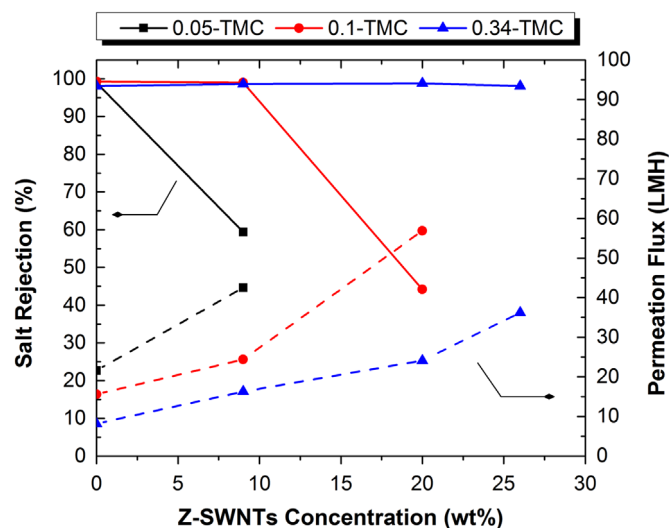


Fig. 8. Trade-off between the density of polyamide skin layer, as controlled by the concentration of the crosslinking agent (TMC) and the concentration of Z-SWNTs embedded in the skin layer. The left axis (solid lines) shows the salt rejection of the TFN membranes, and the right axis (dashed lines) shows the permeation flux of each membrane in units of liter per m^2 per hour (LMH). All the membranes were operated under the same applied transmembrane pressure at 2.41 MPa. The feed solution contained 2000 ppm of Na^+ from dissolved sodium chloride.

units of LMH.

Increasing the concentration of TMC reduces the water permeation in the membrane in the absence of Z-SWNTs, which agrees with results reported by Ahmad et al. [48] that the rate of reaction for polymerization is increased tremendously as the TMC content was increased, reducing the pore size and free volume of the skin layer, and hence lowering the permeation. Plain PA membranes fabricated with 0.05 (v/v)% of TMC had looser polymer chains and larger pore sizes, offering high salt rejection (98.9%) and permeation flux (21.6 LMH). However, when 9 wt% of Z-SWNTs was added into this loose membrane, the rejection decreased drastically to 59%. This shows that the skin layer structure is disrupted by the inclusion of nanotubes. When a higher concentration of TMC was used during the fabrication the PA layer was better able to accommodate high loadings of nanotubes. When the concentration of TMC was increased to 0.34 (v/v)% the skin layer was able to accommodate up to 26 wt% CNT without a significant decrease in salt rejection. Among all the TFN membranes studied, we found the optimal condition to be at 0.34 (v/v)% of TMC and 26 wt% of Z-SWNTs. These conditions resulted in the highest water flux (36.2 LMH) and salt rejection (greater than 98%).

3.4. Feed concentration effects (RO or charged NF)

Holt et al. [10] fabricated nanofiltration (NF) membranes using –COOH functionalized CNTs. Their results show that the salt rejection of the membranes declined drastically when the salt concentration in the feed solution increased from 1 mM to 10 mM. This phenomenon generally occurs in charged NF membranes, where the average pore size of the separation skin layer is significantly larger than the species being separated. In these cases the fixed charges from the functional nanoparticles or acid groups on the polymer backbone induces an electrostatic repulsion to exclude ions of the same charge. This reduces the effective pore size of the membrane, a separation mechanism known as Donnan charge exclusion. However, at higher feed concentrations (i.e. ≥ 2000 ppm) the Donnan exclusion effect is negated by electrostatic screening of the fixed charges. In the case of Holt et al. [10], the Debye length, λ_D , of the charged functional groups on the CNTs decreased as the ionic strength of the solution increased. Salt rejection decreased rapidly when λ_D fell below the CNT diameter.

In our previous simulation and experimental study, zwitterion functionalized SWNTs reject ions via a different separation mechanism than singly-charged functionalized CNTs. Simulations suggested that increasing the feed concentration of NaCl from 0.3 M to 0.6 M would not affect the salt rejection ability of the zwitterion functionalized CNT membranes [17]. The water flux and salt rejection of a 20 wt% Z-SWNT/PA membrane was studied in order to determine whether the Z-SWNT/PA membranes reject ions based on size or Donnan exclusion. The feed solution contains MgSO_4 or MgCl_2 with concentration of Mg^{2+} ranging from 100 to 5000 ppm (4.1 mM to 205.7 mM). We used Mg^{2+} as the feed cation because its divalent charge increases the ionic strength much faster than a monovalent salt and retards Donnan exclusion rapidly. As shown in Fig. 9, the overall salt rejection for Mg^{2+} stayed above 97% and varied only by $\pm 1\%$ between different membrane samples. The rejection increased slightly as the feed concentration increased for both MgSO_4 and MgCl_2 , and was as high as 99.7% even at the highest feed concentration of 5000 ppm. This indicates that the effective pore size of Z-SWNTs remains unchanged regardless of the ionic strength of the feed. In other words, the electrostatic screening due to dissolved salt ions does not impact the selectivity of the membrane. There is no significant difference in salt rejection between MgCl_2 and MgSO_4 (Table 3).

Francesco et al. [10] suggest that the larger the valence number

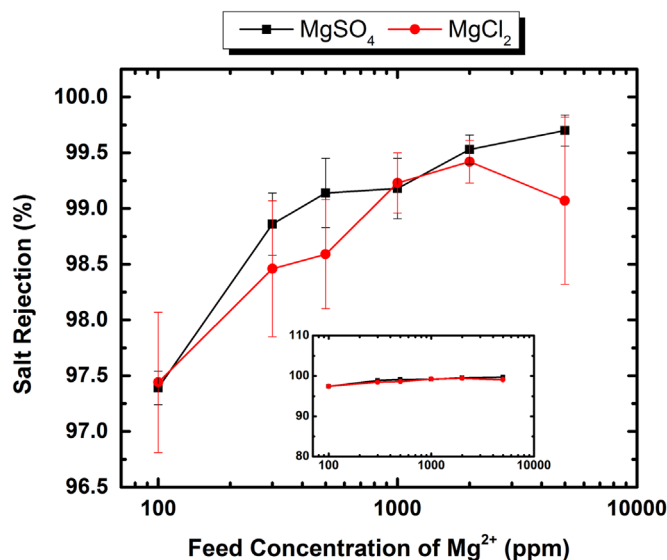


Fig. 9. Salt rejection for MgSO_4 and MgCl_2 as a function of Mg^{2+} concentration in the feed solution. Solution concentration varies from 100 to 5000 mg/L. Three membrane samples of 20 wt% Z-SWNT/PA were tested, and the error bar shows the standard deviation between trials. The applied transmembrane pressure is 2.41 MPa. The secondary plot within the figure shows that the change of salt rejection is relatively small, while the expanded plot enlarges the initial and final drop of the rejection. Corresponding permeation fluxes are given in the Supplementary material.

Table 3
Hydrated radii [49] for the ions tested in this study.

Cation	Hydrated Radii (Å)	Anion	Hydrated Radii (Å)
K^+	3.31	Cl^-	3.32
Na^+	3.58	SO_4^{2-}	3.79
Ca^{2+}	4.12		
Mg^{2+}	4.38		

difference between cation and anion (z^+ and z^-) the better the salt rejection will be for a charged NF membrane. This is because charged membranes will exhibit a stronger repulsive force toward the oppositely charged ions relative to the attractive force to the similarly charged ions. This results in more counterions being rejected by the membrane than co-ions transported through. For a negatively-charged membrane, if the z^-/z^+ ratio in the feed solution decreases from 1 to 0.5 (e.g. CaSO_4 to CaCl_2), the rejection of the cation could drop from approximately 40% to less than 15% [10]. In contrast, the Z-SWNT/PA membrane reported here did not experience any significant reduction in salt rejection when the z^-/z^+ ratio decreased from 1 to 0.5 (MgSO_4 to MgCl_2). This further demonstrates that the electrostatic screening effect is negligible in the Z-SWNTs membranes.

3.5. Permselectivity for common cations

Z-SWNT/PA membranes were also tested using other common alkali ions present in seawater. Plain PA and 20 wt% Z-SWNT/PA membranes were tested for water and ion flux with feed solutions containing 2000 ppm of Na^+ , Mg^{2+} , K^+ or Ca^{2+} cations from NaCl, $\text{MgCl}_2/\text{MgSO}_4$, KCl or CaCl_2 respectively. A second set of experiments was conducted with all the feed solutions maintained at an ionic strength of 87 mM. The permeation flux and ion rejection are shown in Fig. 10. The water flux for all five salt solutions increased approximately three-fold after adding Z-SWNTs to the PA matrix. For example, the water flux increased from 14.7 to 34.7 LMH for the NaCl solution and from 7.4 to 30 LMH for the

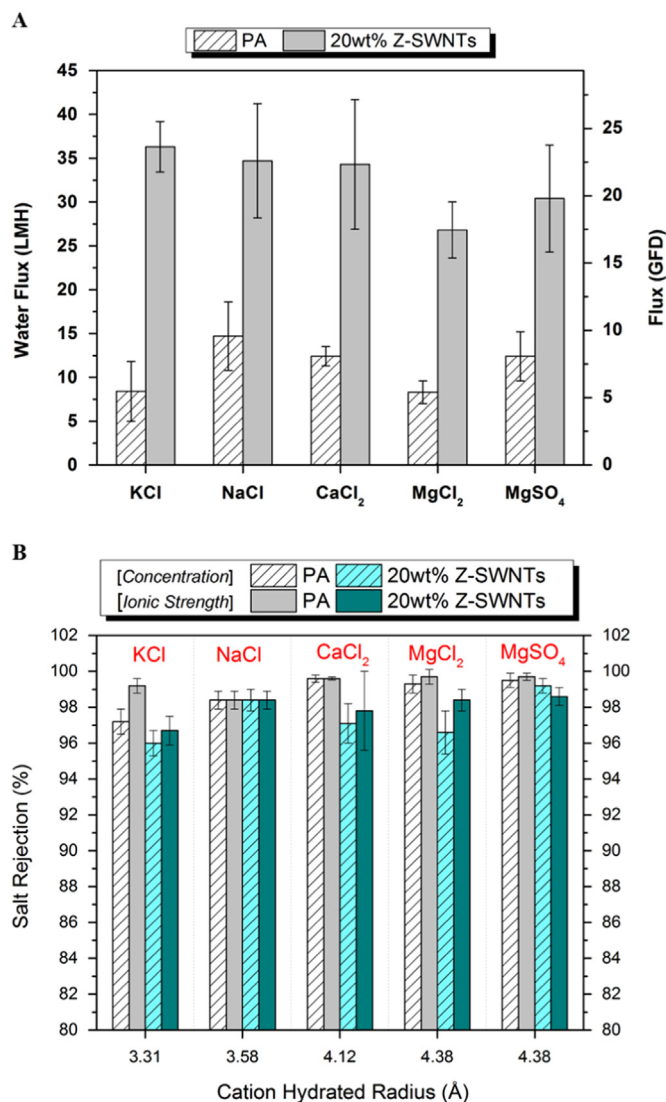


Fig. 10. (A) Permeation flux of plain PA (white hatched) and Z-SWNT/PA membrane (grey solid). All cation concentrations in feed solutions were maintained at 2000 ppm. (B) Salt rejection for both constant cation concentration experiment (Concentration) and constant ionic strength experiment (Ionic strength). Results for PA are shown in white hatch and grey bars. Results for nanocomposite membrane are shown in light cyan with hatch and dark cyan bars. Results are the average of tests on three different membranes. The transmembrane pressure was 2.41 MPa and the feed flow rate was at 2.5 LPM.

MgCl₂ solution. A similar trend was observed in both sets of experiments (i.e. constant concentration and constant ionic strength). Based on our previous study [17], water transport in the Z-SWNT/PA membrane could occur through the core of the nanotubes as well as through “nanochannel” defects at the interface between the CNT outer wall and the polymer matrix. The increase in permeation flux could be due to the presence of either or both of these transport paths. The zwitterionic functional groups used in this study have been demonstrated to have strong water sorption properties [39], which attracts more water to the tip of the CNTs and facilitates water entry into the nanotubes. However, the bulky size of the functional groups was also shown to greatly decrease the water permeation rate in CNTs. If nanochannels are present next to every CNT, water could possibly be transported through them rather than through the CNT cores.

The cation rejection data for different salts with constant feed concentration or ionic strength are shown in Fig. 10(B). The first four salts in the graph have the same anion group (Cl⁻) to allow

for direct comparison. In the plain PA membrane, divalent cations experienced ~1% higher rejection than monovalent cations at the same mass concentration. This could be due to the stronger bonding energy between the divalent metal ions and water molecules in the feed solution, which results in a larger diameter for the hydrated ions. However, this increase in rejection also corresponds to an increase in the ionic strength of the feed solutions. In contrast, the Z-SWNT/PA membrane exhibited no discernible trend in salt rejection with regard to the hydrated radius of the cations, as any differences in the measured rejection values are within the experimental error. In the constant ionic strength experiment, the charge screening effect of the dissolved ions on the membrane is the same for all salt solutions. By factoring out differences in electrostatics, any differences in the rejection should be due to the size sieving and should correlate with the size of the hydrated ions. However, no discernible trend in the cation rejection is observed for the constant ionic strength test in either the PA or Z-SWNT/PA membranes. The nearly constant rejection values (as a function of hydrated radius and ionic strength) suggest that the pores in both the PA and Z-SWNT/PA membranes are smaller than the hydrated radius of the smallest cation (K⁺).

The selectivity of the membranes showed a consistent trend upon the addition of the Z-SWNTs into the PA matrix. The salt rejection values for Na⁺ are identical in the plain PA and nanocomposite membranes. However, the average rejection of Ca²⁺ and Mg²⁺ was slightly higher in the PA membrane than in the Z-SWNT membrane, although this difference was within the experimental error. The addition of Z-SWNT generally increased the variation in selectivity measurements between membranes. This is likely due to the difficulty in achieving consistent orientation, dispersity, and density of Z-SWNTs in the PA film from membrane to membrane, resulting in a larger fluctuation in salt rejection compared to the pure PA membranes. Some of the nanocomposite membranes exhibited Ca²⁺ rejection values as high as 99.3% while others exhibited values below 96%.

During the functionalization of the Z-SWNTs, the zwitterionic functional groups can react both at the CNT ends as well as at reactive defect sites along the length of the CNT. These randomly distributed zwitterionic groups attract polymer chains during the interfacial polymerization via electrostatic interactions and hydrogen bonding, and could serve to decrease the formation of nanochannels outside the CNTs. Molecular simulations by Johnson et al. [17] have shown that zwitterion functionalized CNTs at the tube end can greatly reduce or even stop the transport of ions through the core of CNT, while still allowing acceptable levels of water molecule transport. More than 6000 zwitterionic groups are estimated to react on the outside walls of each CNT. These defect-site zwitterionic groups may also serve to reject ion transport through nanochannels outside the CNTs. Therefore, we can posit three possible paths for selective water transport: through the core of CNTs, through nanochannels outside the CNTs, and through the PA matrix. Other research studies on mixed-matrix membranes agree with this theory that fluid flows through thin-film nanocomposite membranes via these three pathways [50,51]. As discussed previously, when the embedded CNT concentration remains constant, increasing the crosslink density of the PA matrix results in a decrease in the permeation flux. This could be caused by a decrease in the presence of nanochannels due to stronger interactions with the polymer, forcing more water to be transported slowly through the PA matrix. In addition, the diffusivity in the polymer matrix decreases with increasing crosslink density, so any water transport through the PA matrix is further slowed. The lack of change in salt rejection upon the addition of CNTs suggests that the combination of the three transport mechanisms present in the Z-SWNT/PA membranes results in a pore size distribution similar to that of the PA membranes.

3.6. Pore size distribution of thin film nanocomposite membrane

Water and salt ions are commonly understood to permeate through nonporous polymeric films via a solution-diffusion mechanism. However, some studies show that RO membranes can be treated as a porous separator with sub-nanometer pores created by irregular packing of randomly kinked stiffed chains [52]. These voids are interconnected and form tortuous channels 0.6 to 0.9 nm in diameter, through which the majority of water flows. Only 1% of the water is carried by homogeneous diffusion in the polymer matrix [53]. The Z-SWNT/PA membranes contain CNTs that act as channels for water flux, so it is reasonable to describe the transport using the pore flow model. Both the pore size and pore size distribution (PSD) are of interest, as they could give insight into the presence of defects (i.e. nanochannels outside the CNTs). The pore size and PSD were determined based on the permeation of a series of uncharged solutes with known molecular size (the molecular radii of the solutes are listed in Table S1). The uncharged solutes have no specific interactions with the membrane constituents, and their retention behavior was assumed to be a result of size exclusion only. In addition, the rejection of a given solute was assumed to be equal to the fraction of hydrated pores in the membranes that were smaller than the molecular size of the organic solute. Otero et al. [45] derived the correlation between the actual membrane pore size and the Stokes' radii of the solute used, and the results showed that the pore radius is, on average, 0.14 nm greater than the solute radii (see Supplementary material). This is the closest approach distance between a solute and the pore walls and can be interpreted as the thickness of hydration layer of the pore. Wang et al. [54] have suggested that the pore radius is equal to the Stokes' radii of the rejected solutes, and that there is no hydration layer present in the pores. Based on these assumptions, the PSD curve was obtained by fitting the rejection of the solutes to Eq. (2).

The cumulative PSD and the corresponding PSD for plain PA and Z-SWNT/PA are shown in Fig. 11(A) and (B), respectively. There is no significant difference in the pore size distribution curves between PA and Z-SWNT/PA, and their average pore radii are both around 3.1 Å. The PSD of Z-SWNT/PA calculated without the hydration layer of the pore walls is also shown in Fig. 11. The average pore radius in this case is approximately 1.7 Å. In either case, the pore size did not change after adding Z-SWNTs into the PA matrix, and the effective pore size of the Z-SWNT and its surrounding nanochannels is very similar to the pore size of the PA matrix. In other words, the zwitterionic groups at the tip of the CNT have reduced the effective pore size from an initial diameter of 15 Å to ~3.1 Å. This result agrees with the ion rejection measurements, where similar values of salt rejection were observed for both PA and Z-SWNT/PA membranes. The primary difference between the membranes is the geometry of the pores: water and ions travel through tortuous and interconnected nanovoids in the PA matrix, but in straighter and more continuous CNT cores and nanochannels in the Z-SWNT/PA membrane. Another possible explanation is that most of the sieving of the uncharged solutes occurs in a layer of PA covering the CNTs, and the CNTs then provide fast channels for water permeation after the sieving occurs. All the permeation fluxes in this experiment increased significantly when the CNT content in the film increased. However, it is unclear whether the ends of the Z-SWNTs pierce the upper surface of the membrane, so the selectivity could be due to a thin PA top layer. This would account for the similar salt rejection values observed in the PA and Z-SWNT/PA membranes.

3.7. Analysis of surface biofouling

The surface biofouling behavior of the PA and Z-SWNT/PA

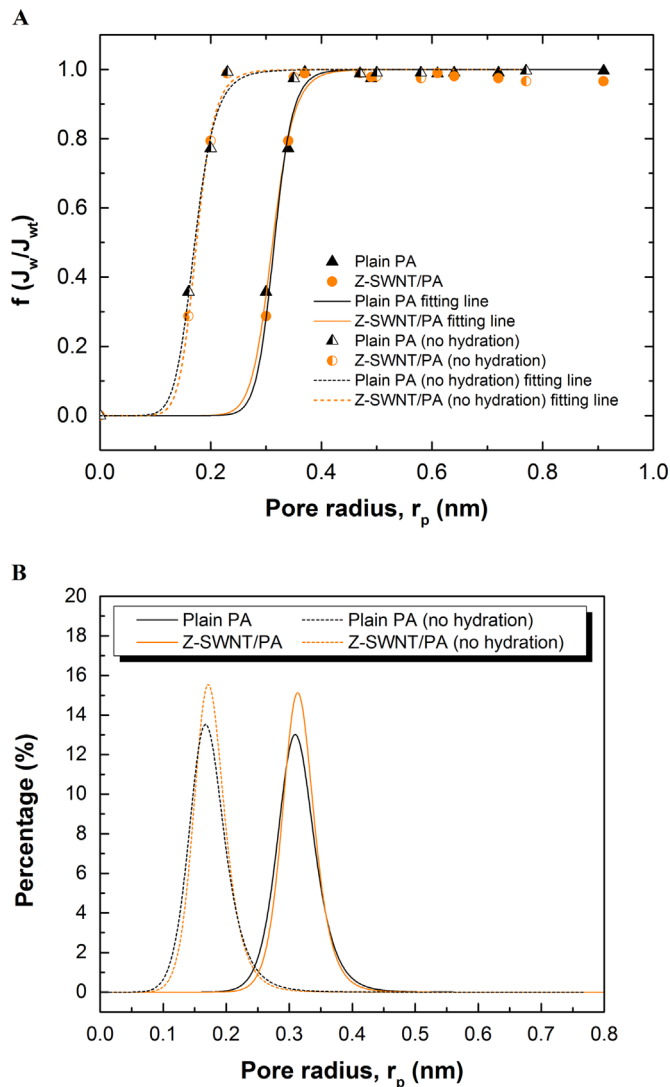


Fig. 11. (A) Solute rejection ($f(J_w/J_{wt})$) as a function of pore radius, r_p . (B) Pore size distribution (percent of pores with a given r_p) calculated from the derivatives of the solute rejection plots in (A).

membranes was studied by exposing the membranes to a bovine serum albumin (BSA) solution and measuring the decrease in water flux over time. Exposed zwitterionic groups on the functionalized CNTs are expected to improve the surface biofouling properties of the Z-SWNT/PA membranes. Zwitterions, possessing both positive and negative charges, create stronger and more stable electrostatic interactions with water than uncharged hydrophilic materials. This results in a hydration layer at the membrane surface and makes it difficult for foulants to displace water molecules and bind to the surface. Polyamide RO membranes possess surface charges [55] due to the presence of carboxylic groups on the polymer backbone. Common foulant species (e.g. proteins) are also charged in solution and are thus attracted to the membranes and can bind strongly due to specific interactions between functional groups, an effect that increases surface fouling [46]. We expect that the PA surface studied here had a low surface charge due to the high degree of chemical crosslinking in the film [48], making it is less prone to foulant adsorption. The conditions of the feed solution, therefore, were adjusted to enhance the fouling ability of the BSA in solution. Elimelech et al. [46] reported that increasing the ionic strength in the feed solution reduces the electrostatic repulsion between BSA molecules and between the BSA molecules and the membrane. The addition of calcium ion to

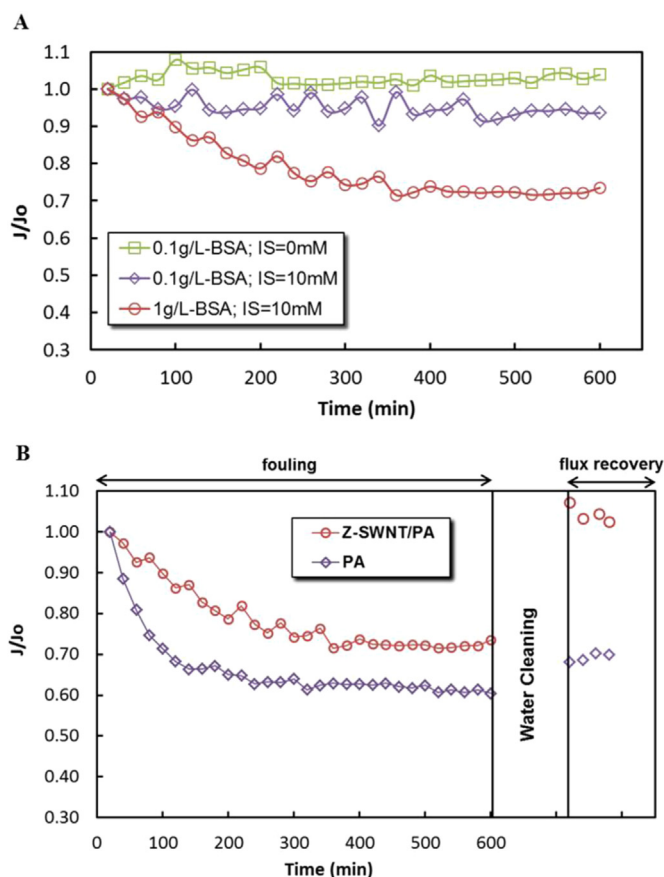


Fig. 12. Normalized flux of the membranes as a function of time during BSA fouling. (A) Effect of ionic strength (IS) and BSA concentration on fouling of 20 wt% Z-SWNT/PA membrane. Total ionic strength of the feed solution was adjusted by varying Ca^{2+} and NaCl concentration. (B) Comparison of flux change between the control PA and nanocomposite membranes. The concentration of BSA was kept at 1 g/L, and the solution pH was constantly adjusted to 4.7. AAS (100 mg/L) was added to the solution during each test.

the feed solution also promotes the formation of complexes composed of the constituent of organic foulants and then assists with BSA adsorption. In our study, 2.0 mM of Ca^{2+} and 4.0 mM of NaCl were added to the feed solution to make up a total ionic strength of 10 mM. The electrostatic repulsion between BSA molecules is further reduced when the pH of the solution is close to the isoelectric point of BSA. Thus, the pH of the feed solution was maintained at 4.7, the isoelectric point of BSA when the ionic strength is 10 mM.

A 20 wt% Z-SWNT/PA membrane was placed in the filtration system, and the permeation flux was recorded every 20 min over the course of 10 h. The membrane was then flushed with pure DI water for 2 h before the permeation was tested again. The results are shown in Fig. 12, where the y-axis shows the ratio of the flux, J , to the initial flux, J_0 . The effect of ionic strength and the concentration of BSA can be seen in Fig. 12A, while the flux recovery rate of the membranes is depicted in Fig. 12B. There was no significant decline in permeation fluxes at low concentrations of BSA (0.1 g/L). When the ionic strength in solution increased, the flux decreased slightly and fluctuated, but stayed above 90% of the initial flux. This suggests that some BSA was deposited on the surface but that the adsorption rate was slow due to the low BSA concentration in solution, and the adsorbed BSA could be easily displaced by the crossflow in the system. Significant decreases in permeation were only observed when the concentrations of BSA were greater than 1.0 g/L (flux data for additional operating conditions can be found in the [Supplementary material](#)). A 1.0 g/L

solution of BSA was then used to foul both the PA and Z-SWNT/PA membranes (Fig. 12B). Both membranes exhibited two stages of fouling: at short times, the flux of the plain PA membrane decreased rapidly; after 100 min the rate of flux decrease gradually slowed down and the flux reached a quasi-steady state at a relative flux of $J/J_0 \sim 0.61$. In contrast, the Z-SWNT/PA membrane exhibited a slower loss of flux at short times (less than 300 min) before plateauing at a higher relative flux value ($J/J_0 \sim 0.72$). Thus, the initial adsorption of BSA on the PA membrane surface is faster than on the Z-SWNT/PA surface, and the flux reduction due to fouling is decreased for the Z-SWNT/PA membrane.

The PA membrane retained 60% of its initial flux after 10 h of fouling, whilst the Z-SWNT/PA membrane retained 70% of its initial flux. After the DI-water cleaning procedure, the PA membrane flux returned to a value of 69% of the initial flux, whereas the Z-SWNT/PA membrane flux returned to 100% of the initial flux. The observed water flux in the Z-SWNT/PA membrane after cleaning was slightly higher than the initial flux, and this is attributed to a slight drift in the feed temperature and applied transmembrane pressure. Although both PA and Z-SWNT/PA membranes lost 30–40% of their initial flux due to surface fouling, the recovery of flux in the Z-SWNT/PA membrane indicates that BSA is only weakly adsorbed and is easily removed. This result agrees with reports that surfaces functionalized by zwitterionic group exhibited slower flux reduction rates during fouling and high water flux recovery after washing with clean water [37].

4. Conclusion

A novel nanocomposite desalination membrane was fabricated using zwitterionic functionalized carbon nanotubes incorporated into a polyamide thin film composite. The CNTs in the polyamide layer offer channels for fast water transport, and maintain high salt rejection due to the steric hindrance of the zwitterionic groups located at the ends of the CNTs. The mechanical stability of the polyamide matrix can be improved by increasing the degree of chemical crosslinking. In this way, nanocomposite membranes can be produced with high CNT loadings without introducing defects that lead to decreased salt rejection. The pore size distribution of the nanocomposite membrane was found to be very similar to that of a pure polymer membrane, indicating that the pores created by the functionalized CNTs in the polymer matrix have effective sizes similar to the original polyamide membrane. The flux improvement in the nanocomposite membranes is due to the reduced tortuosity and increased interconnectivity of the water transport channels created by the inclusion of CNTs. The nanocomposite membranes exhibited increased surface fouling resistance, likely due to zwitterionic groups exposed at the membrane surface interacting with the water molecules to prevent strong binding of the foulant. After washing, the nanocomposite membrane regained 100% of the original water flux, indicating that foulants were not strongly adsorbed on the hydrated surface and were easily removed when flushed with clean water. We have demonstrated that advanced materials like CNTs can be synthesized with desired functional groups, and can be embedded into traditional RO membranes to simultaneously resolve the challenge of low flux and surface fouling in the current desalination process.

Acknowledgments

The authors would like to thank Jody Smiley for her help in the AAS and TOC measurements. We also like to acknowledge Dr. Karl Johnson from the Department of Chemical and Petroleum

Engineering at University of Pittsburgh for his writing assistance and proof reading of this article. We gratefully appreciate the Graduate School Assembly at Virginia Tech for financial support of this project.

Appendix A. Supplementary material

Supplementary data associated with this article can be found in the online version at <http://dx.doi.org/10.1016/j.memsci.2016.02.014>.

References

- [1] K.P. Lee, T.C. Arnot, D. Mattia, A review of reverse osmosis membrane materials for desalination—development to date and future potential, *J. Membr. Sci.* 370 (2011) 1–22, <http://dx.doi.org/10.1016/j.memsci.2010.12.036>.
- [2] M. Elimelech, W. Phillip, The future of seawater desalination: energy, technology, and the environment, *Science* 333 (2011) 712–718.
- [3] T. Mezher, H. Fath, Z. Abbas, A. Khaled, Techno-economic assessment and environmental impacts of desalination technologies, *Desalination* 266 (2011) 263–273, <http://dx.doi.org/10.1016/j.desal.2010.08.035>.
- [4] J. Wang, D.S. Dlamini, A.K. Mishra, M.T.M. Pendergast, M.C.Y. Wong, B. B. Mamba, et al., A critical review of transport through osmotic membranes, *J. Membr. Sci.* 454 (2014) 516–537, <http://dx.doi.org/10.1016/j.memsci.2013.12.034>.
- [5] J. Yin, B. Deng, Polymer-matrix nanocomposite membranes for water treatment, *J. Membr. Sci.* 479 (2014) 256–275, <http://dx.doi.org/10.1016/j.memsci.2014.11.019>.
- [6] J.E. Cadotte, R.J. Petersen, R.E. Larson, E.E. Erickson, A new thin-film composite seawater reverse osmosis membrane, *Desalination* 32 (1980) 25–31, [http://dx.doi.org/10.1016/S0011-9164\(00\)86003-8](http://dx.doi.org/10.1016/S0011-9164(00)86003-8).
- [7] T.A. Saleh, V.K. Gupta, Synthesis and characterization of alumina nano-particles polyamide membrane with enhanced flux rejection performance, *Sep. Purif. Technol.* 89 (2012) 245–251, <http://dx.doi.org/10.1016/j.seppur.2012.01.039>.
- [8] E.S. Kim, G. Hwang, M. Gamal El-Din, Y. Liu, Development of nanosilver and multi-walled carbon nanotubes thin-film nanocomposite membrane for enhanced water treatment, *J. Membr. Sci.* 394–395 (2012) 37–48, <http://dx.doi.org/10.1016/j.memsci.2011.11.041>.
- [9] S. Lee, H. Kim, R. Patel, S.J. Im, J.H. Kim, B.R. Min, Silver nanoparticles immobilized on thin film composite polyamide membrane: characterization, nanofiltration, antifouling properties, *Polym. Adv. Technol.* 18 (2007) 562–568, <http://dx.doi.org/10.1002/pat>.
- [10] F. Fornasiero, H.G. Park, J.K. Holt, M. Stadermann, C.P. Grigoropoulos, A. Noy, et al., Ion exclusion by sub-2-nm carbon nanotube pores, *Proc. Natl. Acad. Sci. USA* 105 (2008) 17250–17255, <http://dx.doi.org/10.1073/pnas.0710437105>.
- [11] J.K. Holt, H.G. Park, Y. Wang, M. Stadermann, A.B. Artyukhin, C. P. Grigoropoulos, et al., Fast mass transport through sub-2-nanometer carbon nanotubes, *Science* 312 (2006) 1034–1037, <http://dx.doi.org/10.1126/science.1126298>.
- [12] J.K. Holt, Carbon nanotubes and nanofluidic transport, *Adv. Mater.* 21 (2009) 3542–3550, <http://dx.doi.org/10.1002/adma.200900867>.
- [13] A. Kalra, S. Garde, G. Hummer, Osmotic water transport through carbon nanotube membranes, *Proc. Natl. Acad. Sci. USA* 100 (2003) 10175–10180, <http://dx.doi.org/10.1073/pnas.1633354100>.
- [14] B. Corry, Designing carbon nanotube membranes for efficient water desalination, *J. Phys. Chem. B* 112 (2008) 1427–1434, <http://dx.doi.org/10.1021/jp709845u>.
- [15] C. Song, B. Corry, Intrinsic ion selectivity of narrow hydrophobic pores, *J. Phys. Chem. B* 113 (2009) 7642–7649, <http://dx.doi.org/10.1021/jp810102u>.
- [16] B. Corry, Water and ion transport through functionalised carbon nanotubes: implications for desalination technology, *Energy Environ. Sci.* 4 (2011) 751, <http://dx.doi.org/10.1039/c0ee00481b>.
- [17] W.-F. Chan, H. Chen, A. Surapathi, J.K. Johnson, E. Marand, et al., Zwitterion functionalized carbon nanotube/polyamide nanocomposite membranes for water desalination, *ACS Nano* 7 (2013) 5308–5319.
- [18] H. Kim, K. Choi, Y. Baek, D. Kim, High-performance reverse osmosis CNT/polyamide nanocomposite membrane by controlled interfacial interactions, *ACS Appl. Mater. Interfaces* (2014) 2819–2829.
- [19] H. Ma, K. Yoon, L. Rong, M. Shokralla, A. Kopot, X. Wang, et al., Thin-film nanofibrous composite ultrafiltration membranes based on polyvinyl alcohol barrier layer containing directional water channels, *Ind. Eng. Chem. Res.* 49 (2010) 11978–11984, <http://dx.doi.org/10.1021/ie100545k>.
- [20] S. Kim, F. Fornasiero, H.G. Park, J. Bin In, E. Meshot, G. Giraldo, et al., Fabrication of flexible, aligned carbon nanotube/polymer composite membranes by in-situ polymerization, *J. Membr. Sci.* 460 (2014) 91–98, <http://dx.doi.org/10.1016/j.memsci.2014.02.016>.
- [21] M. Majumder, N. Chopra, B.J. Hinds, Mass transport through carbon nanotube membranes in three different regimes: ionic diffusion and gas and liquid flow, *ACS Nano* 5 (2011) 3867–3877, <http://dx.doi.org/10.1021/nn200222g>.
- [22] A.I. Skoulidas, D.M. Ackerman, J.K. Johnson, D.S. Sholl, Rapid transport of gases in carbon nanotubes, *Phys. Rev. Lett.* 89 (2002) 185901.
- [23] J. Park, W. Choi, S.H. Kim, B.H. Chun, J. Bang, K.B. Lee, Enhancement of chlorine resistance in carbon nanotube based nanocomposite reverse osmosis membranes, *Desalination Water Treat.* 15 (2010) 198–204, <http://dx.doi.org/10.5004/dwt.2010.1686>.
- [24] D. Rana, Y. Kim, T. Matsuura, H.A. Arafat, Development of antifouling thin-film-composite membranes for seawater desalination, *J. Membr. Sci.* 367 (2011) 110–118, <http://dx.doi.org/10.1016/j.memsci.2010.10.050>.
- [25] G.L. Jadao, P.S. Singh, Synthesis of novel silica-polyamide nanocomposite membrane with enhanced properties, *J. Membr. Sci.* 328 (2009) 257–267, <http://dx.doi.org/10.1016/j.memsci.2008.12.014>.
- [26] M.L. Lind, B.-H. Jeong, A. Subramani, X. Huang, E.M.V. Hoek, Effect of mobile cation on zeolite-polyamide thin film nanocomposite membranes, *J. Mater. Res.* 24 (2009) 1624–1631, <http://dx.doi.org/10.1557/jmr.2009.0189>.
- [27] L. Zhang, G.-Z. Shi, S. Qiu, L.-H. Cheng, H.-L. Chen, Preparation of high-flux thin film nanocomposite reverse osmosis membranes by incorporating functionalized multi-walled carbon nanotubes, *Desalination Water Treat.* 34 (2011) 19–24, <http://dx.doi.org/10.5004/dwt.2011.2801>.
- [28] S. Kim, S. Kwak, T. Suzuki, Positron annihilation spectroscopic evidence to demonstrate the flux-enhancement mechanism in morphology-controlled thin-film-composite (TFC) membrane, *Environ. Sci. Technol.* 39 (2005) 1764–1770.
- [29] W. Xie, G.M. Geise, B.D. Freeman, H.-S. Lee, G. Byun, J.E. McGrath, Polyamide interfacial composite membranes prepared from m-phenylene diamine, trimethylchloride and a new disulfonated diamine, *J. Membr. Sci.* (2012), <http://dx.doi.org/10.1016/j.memsci.2012.02.038>.
- [30] C.-F. de Lannoy, D. Jassby, K. Gloe, A.D. Gordon, M.R. Wiesner, Aquatic bio-fouling prevention by electrically charged nanocomposite polymer thin film membranes, *Environ. Sci. Technol.* (2013), <http://dx.doi.org/10.1021/es3045168>.
- [31] E.M.V. Hoek, Y. Yan, B. Jeong, Nanocomposite Membranes and Methods of Making and Using Same, WO Patent 2,006,098,872. 1, 2006.
- [32] M.L. Lind, A.K. Ghosh, A. Jawor, X. Huang, W. Hou, Y. Yang, et al., Influence of zeolite crystal size on zeolite-polyamide thin film nanocomposite membranes, *Langmuir: ACS J. Surf. Colloids* 25 (2009) 10139–10145, <http://dx.doi.org/10.1021/la900938x>.
- [33] H.S. Lee, S.J. Im, J.H. Kim, H.J. Kim, J.P. Kim, B.R. Min, Polyamide thin-film nanofiltration membranes containing TiO₂ nanoparticles, *Desalination* 219 (2008) 48–56, <http://dx.doi.org/10.1016/j.desal.2007.06.003>.
- [34] J. Duan, E. Litwiller, I. Pinnau, Preparation and water desalination properties of POSS-polyamide nanocomposite reverse osmosis membranes, *J. Membr. Sci.* 473 (2015) 157–164, <http://dx.doi.org/10.1016/j.memsci.2014.09.022>.
- [35] G. Cheng, G. Li, H. Xue, S. Chen, J.D. Bryers, S. Jiang, Zwitterionic carboxybetaine polymer surfaces and their resistance to long-term biofilm formation, *Biomaterials* 30 (2009) 5234–5240, <http://dx.doi.org/10.1016/j.biomaterials.2009.05.058>.
- [36] S. Jiang, Z. Cao, Ultralow-fouling, functionalizable, and hydrolyzable zwitterionic materials and their derivatives for biological applications, *Adv. Mater.* (2010).
- [37] S. Azari, L. Zou, Using zwitterionic amino acid L-DOPA to modify the surface of thin film composite polyamide reverse osmosis membranes to increase their fouling resistance, *J. Membr. Sci.* 401–402 (2012) 68–75, <http://dx.doi.org/10.1016/j.memsci.2012.01.041>.
- [38] Nano Lab Inc., 179 Bear Hill Road, Waltham, MA 02451, n.d.
- [39] A. Surapathi, H. Chen, E. Marand, J. Karl Johnson, Z. Sedlakova, Gas sorption properties of zwitterion-functionalized carbon nanotubes, *J. Membr. Sci.* 429 (2013) 88–94, <http://dx.doi.org/10.1016/j.memsci.2012.11.021>.
- [40] Z. Zhang, S. Chen, S. Jiang, Dual-functional biomimetic materials: nonfouling poly(carboxybetaine) with active functional groups for protein immobilization, *Biomacromolecules* 7 (2006) 3311–3315, <http://dx.doi.org/10.1021/bm060750m>.
- [41] A.K. Ghosh, E.M.V. Hoek, Impacts of support membrane structure and chemistry on polyamide-polysulfone interfacial composite membranes, *J. Membr. Sci.* 336 (2009) 140–148, <http://dx.doi.org/10.1016/j.memsci.2009.03.024>.
- [42] N.K. Saha, S.V. Joshi, Performance evaluation of thin film composite polyamide nanofiltration membrane with variation in monomer type, *J. Membr. Sci.* 342 (2009) 60–69, <http://dx.doi.org/10.1016/j.memsci.2009.06.025>.
- [43] C. Kong, M. Kanezashi, T. Yamamoto, T. Shintani, T. Tsuru, Controlled synthesis of high performance polyamide membrane with thin dense layer for water desalination, *J. Membr. Sci.* 362 (2010) 76–80, <http://dx.doi.org/10.1016/j.memsci.2010.06.022>.
- [44] S. Kim, J.R. Jinschek, H. Chen, D.S. Sholl, E. Marand, Scalable fabrication of carbon nanotube/polymer nanocomposite membranes for high flux gas transport, *Nano Lett.* 7 (2007) 2806–2811, <http://dx.doi.org/10.1021/nl071414u>.
- [45] J.A. Otero, O. Mazarrasa, J. Villasante, V. Silva, P. Prádanos, J.I. Calvo, et al., Three independent ways to obtain information on pore size distributions of nanofiltration membranes, *J. Membr. Sci.* 309 (2008) 17–27, <http://dx.doi.org/10.1016/j.memsci.2007.09.065>.
- [46] W. Ang, M. Elimelech, Protein (BSA) fouling of reverse osmosis membranes: implications for wastewater reclamation, *J. Membr. Sci.* 296 (2007) 83–92, <http://dx.doi.org/10.1016/j.memsci.2007.03.018>.
- [47] R.J. Petersen, J.E. Cadotte, Thin film composite reverse osmosis membranes, *Handbook of Industrial Membrane Technology*, 1990, pp. 307–348.

- [48] A. Ahmad, B. Ooi, Properties–performance of thin film composites membrane: study on trimesoyl chloride content and polymerization time, *J. Membr. Sci.* 255 (2005) 67–77, <http://dx.doi.org/10.1016/j.memsci.2005.01.021>.
- [49] E.R. Nightingale, Phenomenological theory of ion solvation. Effective radii of hydrated ions, *J. Phys. Chem.* 63 (1959) 1381–1387, <http://dx.doi.org/10.1021/j150579a011>.
- [50] S. Turgman-Cohen, J.C. Araque, E.M.V. Hoek, F.A. Escobedo, Molecular dynamics of equilibrium and pressure-driven transport properties of water through LTA-type zeolites, *Langmuir* 29 (2013) 12389–12399, <http://dx.doi.org/10.1021/la402895h>.
- [51] P. Cay-Durgun, S.G. Fink, A. Shabilla, H. Yin, K.A. Sasaki, M.L. Lind, Analysis of the water permeability of linde type A zeolites in reverse osmosis, *Sep. Sci. Technol.* 49 (2014) 2824–2833, <http://dx.doi.org/10.1080/01496395.2014.946147>.
- [52] K. Košutić, L. Kaštelan-Kunst, B. Kunst, Porosity of some commercial reverse osmosis and nanofiltration polyamide thin-film composite membranes, *J. Membr. Sci.* 168 (2000) 101–108.
- [53] K. Chan, T. Liu, Effect of shrinkage on pore size and pore size distribution of cellulose acetate reverse osmosis membranes, *Ind. Eng. Chem.* (1984) 124–133.
- [54] X. Wang, D. Fang, B.S. Hsiao, B. Chu, Nanofiltration membranes based on thin-film nanofibrous composites, *J. Membr. Sci.* 469 (2014) 188–197, <http://dx.doi.org/10.1016/j.memsci.2014.06.049>.
- [55] M. Hadidi, A.L. Zydney, Fouling Behavior of Zwitterionic Membranes: Impact of Electrostatic and Hydrophobic Interactions, *J. Membr. Sci.*, Elsevier (2013) <http://dx.doi.org/10.1016/j.memsci.2013.09.062>.